Review — Research and Development of Titanium-Containing Biomedical High Entropy Alloys (BioHEAs) Utilizing Rapid Solidification via Laser-Powder Bed Fusion[*1]

Ryosuke Ozasa[1,2], Aira Matsugaki[1,2], Takuya Ishimoto[1,2,3] and Takayoshi Nakano[1,2,*2]

[1]*Division of Materials and Manufacturing Science, Graduate School of Engineering, Osaka University, Suita 565-0871, Japan*
[2]*Anisotropic Design and Additive Manufacturing Research Center, Osaka University, Suita 565-0871, Japan*
[3]*Aluminium Research Center, University of Toyama, Toyama 930-8555, Japan*

High entropy alloys (HEAs) have been developed as a new class of structural materials that consist of multicomponent elements with an approximately equiatomic ratio for increasing the mixing entropy to stabilize the solid solution phase. HEA for biomedical applications (BioHEA) was first developed in Japan; HEA comprising nonbiotoxic elements was specifically designed, demonstrating excellent mechanical properties and biocompatibility. However, elemental segregation, often observed in BioHEAs, hinders the inherent functions derived from high entropy effects and solid solution hardening. In this review article, elemental homogenization and functionalization of BioHEAs utilized by ultra-rapid cooling via laser-powder bed fusion and the characteristics of these BioHEAs, especially focusing on their excellent properties for biomedical applications, are introduced.   [doi:10.2320/matertrans.MT-MLA2022011]

1. Introduction

High entropy alloys (HEAs)[1,2] have attracted worldwide attention as novel alloy systems with excellent functions. HEAs are multicomponent alloys containing a combination of five or more elements and do not have a specific solvent. They are expected to exhibit superior nonlinear functionality via solid solution formation by increasing the entropy of mixing. In 2017, our group proposed an equiatomic Ti–Zr–Nb–Ta–Mo alloy as the first HEA for biomedical applications (BioHEA) that does not contain biotoxic elements.[3–6] Subsequently, the research group developed the Ti–Zr–Hf–Y–La system,[7] Ti–Zr–Hf–(Co)–Cr–Mo system,[8] and Ti–Zr–Hf–Nb–Ta–Mo system.[9] BioHEAs are being actively studied and developed worldwide.[10–14]

BioHEAs manufactured using the casting method exhibit mechanical properties and biocompatibility equal to or better than those of conventional metal biomaterials. However, there is a strong tendency toward phase separation based on elemental segregation. Moreover, a uniform solid solution is not obtained for the cast materials. Therefore, the function of HEAs, which should be uniform solid solutions, cannot always be expressed (Fig. 1). Functional deterioration due to phase separation has been reported not only in BioHEAs but also in other systems of HEAs (e.g., Fe–Co–Ni–Cr–Cu and Fe–Ni–Cr–Mn–Cu).[15–17] This implies that the suppression of phase separation and formation of solid solution are common issues in HEAs in general.

This review paper presents the research results and knowledge of our group on the expression of high functionality based on the suppression of elemental homogenization and solid solution formation of BioHEAs using laser-powder bed fusion (L-PBF), which is one of the
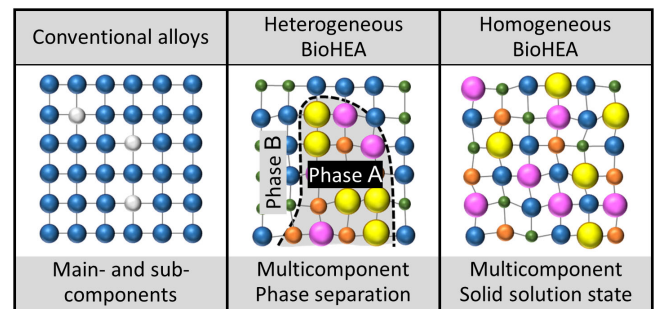

Fig. 1   Schematic drawing of atomic arrangement in conventional alloys, heterogeneous high entropy alloy for biomedical applications (BioHEA) with phase separation, and homogeneous uniform solid solution state of BioHEA.

metal additive manufacturing (AM) methods, as an ultra-rapid cooling method in recent years.

2. Phase Separation via Elemental Segregation in BioHEAs Manufactured by Casting

BioHEAs are characterized by their constituent elements, which are less harmful to the body. The combination of elemental species and composition are mainly designed based on the prediction of solid solution formation by the parameter method[18,19] and crystal structure prediction based on the valence electron concentration (VEC) theory.[18–20] The parameter method uses the entropy of mixing (ΔS_{mix}), enthalpy of mixing (ΔH_{mix}), delta parameter (δ), and omega parameter (Ω) as indicators. Solid solution formation is expected when $\Delta S_{mix} \geq 1.5\text{R}$, $-20 \leq \Delta H_{mix} \leq 5$, $\delta \leq 6.6$, and $\Omega \geq 1.1$, respectively.[21] When a solid solution is formed from a multicomponent alloy, the number of electrons per atom (*VEC* value) contained in the valence band, including d-electrons, is believed to be useful as an index for predicting the crystal structure of this solid solution. It is empirically
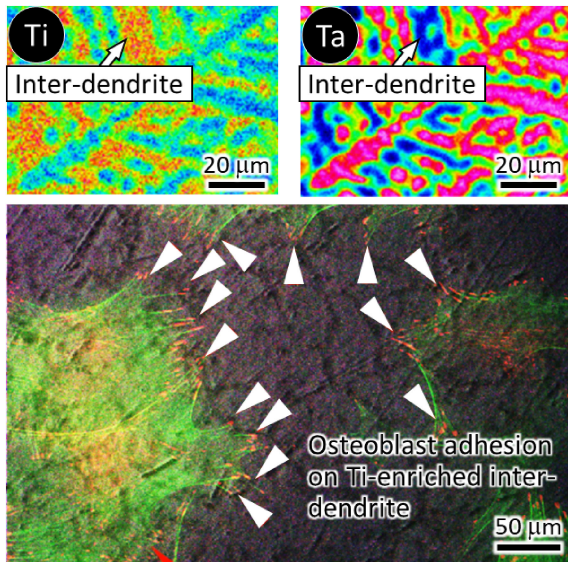

Fig. 2 Elemental segregation and osteoblast adhesion behavior on the cast material of BioHEAs. Osteoblast adhesion sites are confined to Ti-rich inter-dendrite region, leading to reduced cell spreading area.
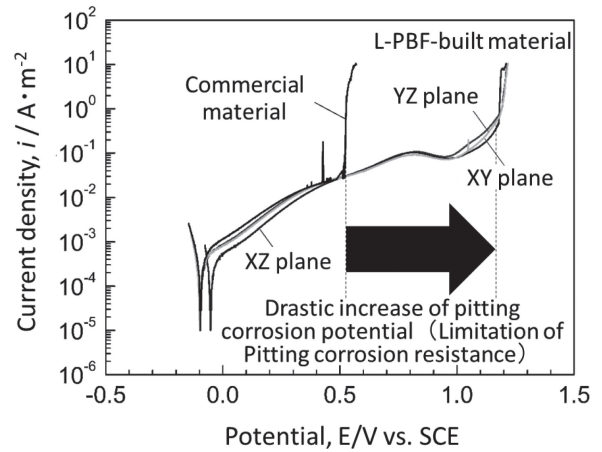

Fig. 3 Increase in pitting corrosion potential in SUS316L stainless steel using ultra-rapid cooling of the L-PBF method. This figure cites Ref. 27) with a minor modification.

known that $VEC \leq 6.87$ results in a single phase of BCC, $6.87 < VEC \leq 8.0$ results in two phases of BCC and FCC, and $8.0 \leq VEC$ results in a single phase of FCC.[20]

In the Ti–Zr–Nb–Ta–Mo-based BioHEAs designed using empirical parameters, each index of the parameter method satisfies the solid solution formation conditions. This BioHEA exhibits a BCC structure in agreement with the prediction by the VEC value. However, phase separation via elemental segregation often occurs in BioHEAs, leading to a heterogeneous elemental distribution that could degrade sophisticated mechanical properties peculiar to them. Moreover, in the cast material of Ti–Zr–Nb–Ta–Mo-based BioHEAs, which exhibit remarkable elemental segregation, osteoblast adhesion is suppressed. The elemental segregation in cast material restricted the filopodia distribution in osteoblasts by holding the adhesion spots in Ti- and Zr-enriched inter-dendrite regions, resulting in the reduced cell spreading area on cast materials (Fig. 2). That is, elemental segregation in the cast material of BioHEAs is not able to completely produce biocompatibility or mechanical functions.

3. Basics of L-PBF as an Ultra-Rapid Solidification Method

In the L-PBF method, which is a type of metal AM, the cooling rate when the metal solidifies reaches a maximum of 10^5–10^7 K/s.[22,23] This rate is immense compared to the cooling rate in conventional metal material fabrication processes, such as the casting method (approximately 100 K/s),[24] centrifugal casting method (100 K/s order),[25] and arc melting method (approximately 2000 K/s).[5] It also exceeds the cooling rate of a single-roll liquid-quenching method for producing amorphous materials (approximately 10^5 K/s).[26] Such ultra-rapid solidification, peculiar to L-PBF, suppresses the elemental segregation/phase separation tendency and can be expected to realize the formation of a uniform single-phase solid solution. In fact, L-PBF realizes the ultra-quenching bulking of SUS316L stainless steel. Further, the metal material exhibits more than twice the pitting potential of commercially available materials and significantly improves pitting corrosion resistance (Fig. 3).[27] Therefore, by applying L-PBF as an ultra-rapid cooling method for the creation of BioHEAs, BioHEAs with a single-phase solid solution is expected to be formed.

The L-PBF method can produce the desired shape with high accuracy.[28,29] Furthermore, it is possible to control the material properties for each location. Living bones are the targets of implanting a biological metal material. Depending on the patient's pathology,[30,31] genetic background,[32] bone type, and sites,[33] not only the shape but also the material properties (including bone mineral density and bone microstructure derived from oriented collagen/apatite) are different for each patient. The L-PBF method has the potential to create metal materials with properties similar to those of living bones that match the skeleton and bone shape of each patient, as well as material properties.

Figure 4(a) schematically shows an example of the procedure used to obtain a three-dimensional material using the L-PBF method. By sweeping the metal raw material powder with a re-coater and irradiating the formed powder bed with a laser beam based on two-dimensional slice data, only the irradiated portion can be selectively melted and solidified. By repeating the melt-solidification process for each layer and stacking two-dimensional objects, a three-dimensional object with an arbitrary shape can be obtained. Laser scanning is controlled by an optical system that includes a condenser lens and a galvanometer mirror in the optical path (Fig. 4(b)). Modeling is mainly performed in an Ar or N_2 atmosphere under a low oxygen concentration of less than 0.1%. Furthermore, by flowing Ar or N_2 gases directly above the modeling stage, fumes generated by laser irradiation are removed. Through laser irradiation, a molten pool is formed by melting metal powder, and controlling its three-dimensional shape and solidification rate leads to the control of the optimal shape and material properties, consequently leading to higher functionality of the manufactured material. The melt solidification behavior of metal
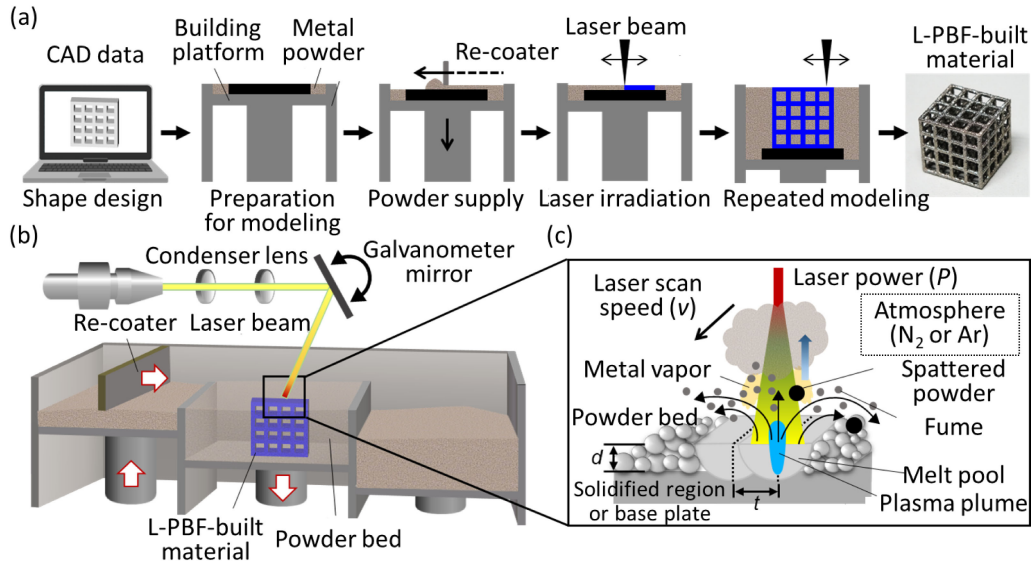
Fig. 4 Schematic illustration of the manufacturing process of a three-dimensional object using the L-PBF method. (a) Shape design using 3D-CAD and following L-PBF building process. (b) Configuration of the L-PBF device. (c) Various building parameters in the L-PBF method.

materials is influenced by various modeling parameters,[34,35] including the wavelength of the laser, physical characteristics and shape of the raw material powder, atmospheric field in the modeling chamber, and other modeling parameters (e.g., laser output power (P [W]), scanning speed (v [m/s]), scanning interval (d [m]), and layer stack thickness (t [m]); Fig. 4(c)). By optimally designing the modeling process considering the energy input determined by these parameters and energy dissipation due to heat transfer and heat conduction, the shape and material properties, such as the crystallographic texture and crystal orientation of the modeling material, can be controlled.[36,37]

4. BioHEAs Manufactured Using the L-PBF Method

In Ti–Zr–Nb–Ta–Mo-based BioHEAs, the non-equiatomic $(TiZr)_{1.4}(NbTaMo)_{0.6}$ alloy, which satisfies the solid solution formation conditions by the parameter method, improves the ductility while maintaining the same yield stress as the equiatomic TiZrNbTaMo alloy.[6] Therefore, if a uniform solid solution can be obtained by applying L-PBF, further improvements in alloy functionality are expected. Figure 5 shows the constituent phases of the raw material powder and L-PBF-built material of the $(TiZr)_{1.4}(NbTaMo)_{0.6}$ alloy analyzed by X-ray diffraction (XRD).[38] Both the raw material powder and L-PBF-built material are commonly composed of the BCC phase (Fig. 5(a)). However, a dendritic structure is observed in the raw material powder; further, remarkable phase separation occurs (Fig. 5(b)). No diffraction peak corresponding to the intermetallic compound is observed, indicating that the $(TiZr)_{1.4}(NbTaMo)_{0.6}$ alloy forms a solid solution with two lattice constants showing the BCC structure. However, L-PBF not only succeeded in producing a jungle-gym structure (Fig. 5(b)) but also exhibits a tendency toward the BCC single phase (Fig. 5(a)).

Figure 6 shows the composition and elemental distribution in cast material and L-PBF-built material of $(TiZr)_{1.4}$-$(NbTaMo)_{0.6}$. The dendrite structure, which is shown by the
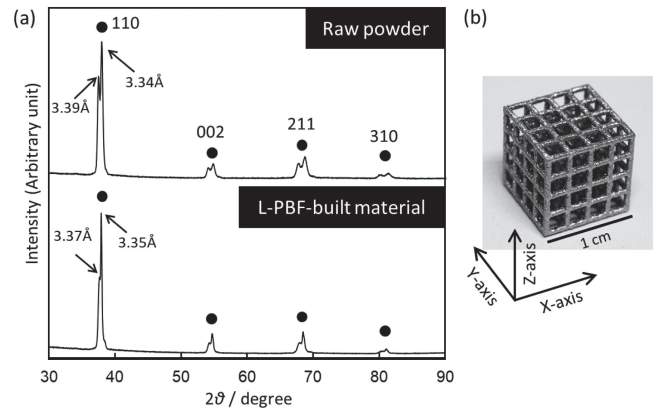

Fig. 5 Suppression of the phase separation and shape control of $(TiZr)_{1.4}(NbTaMo)_{0.6}$ alloy using the L-PBF method. (a) XRD profile for raw powder and L-PBF-built material. (b) Jungle gym-structure fabricated by L-PBF. This figure cites Ref. 38) with a minor modification.
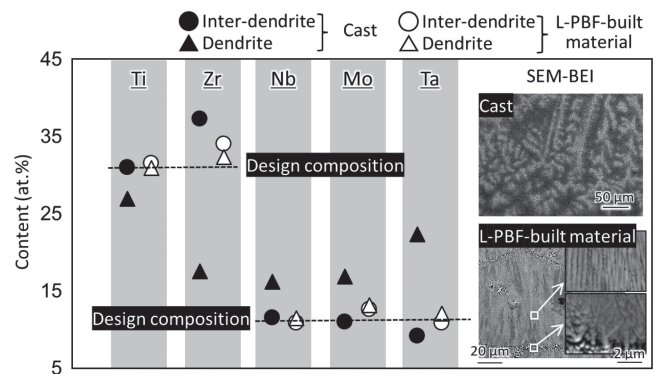

Fig. 6 Suppression of elemental segregation of $(TiZr)_{1.4}(NbTaMo)_{0.6}$ alloy using the L-PBF method. This figure cites Ref. 38) with a minor modification.

white contrast, is developed in the cast material. According to the SEM-EDS analysis, Ta, Mo, and Nb are concentrated in the dendrite region of the cast material, and Ti and Zr are
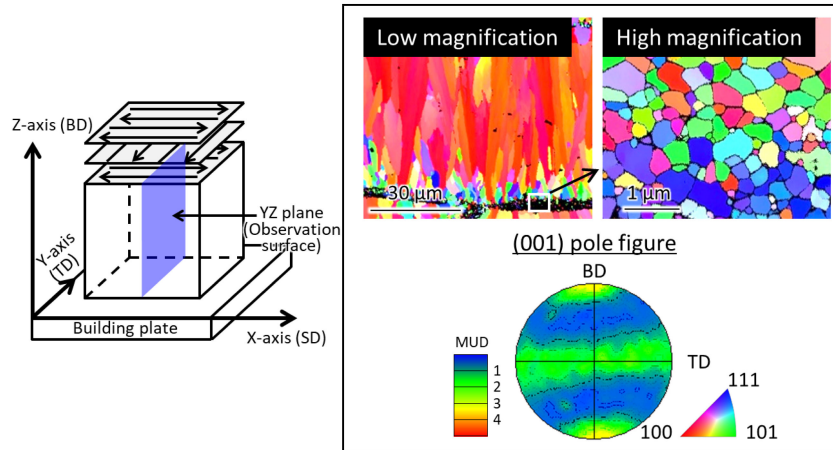
Fig. 7 Schematic diagram of scan strategy XY and crystallographic texture of $(TiZr)_{1.4}(NbTaMo)_{0.6}$ alloy shown by IPF maps and {001} pole figure. The crystal orientation along building direction (BD) is projected in the IPF maps. This figure cites Ref. 38) with a minor modification.
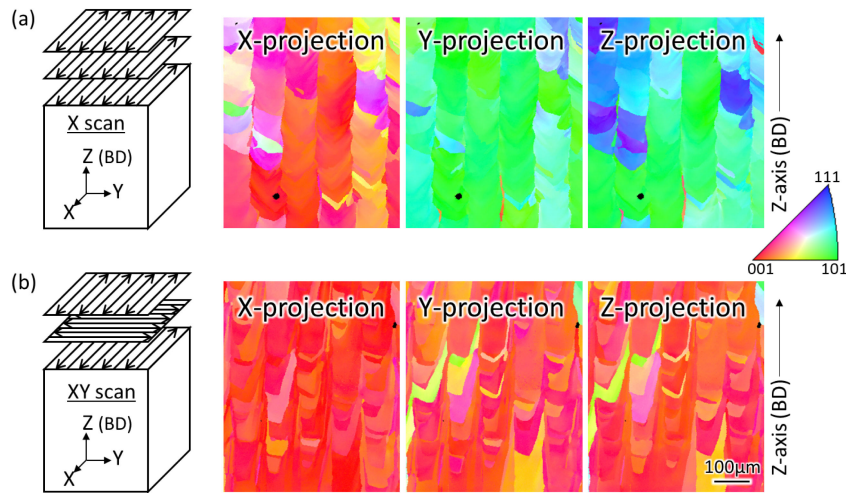

Fig. 8 Crystal orientation control of Ti–15Mo–5Zr–3Al (mass%) using the scan strategy. (a) Scan strategy X. (b) Scan strategy XY. This figure cites Ref. 39) with a minor modification.

concentrated in the inter-dendrite region, which significantly deviate from the design composition.[38] The concentration partition associated with such dendrite formation is consistent with the tendency of the equilibrium partition coefficient.[5] The partition coefficient k ($k = C_s/C_l$, where C_s is solid phase concentration and C_l is liquid phase concentration, when concentrating to liquid phase $k < 1$) of Ti, Zr, and Mo at the liquidus temperature that were calculated using the thermodynamic calculation software FactSage and the thermodynamic database SGTE2017 are 0.60, 0.28, and 1.81, respectively. Although dendrites are observed also in the L-PBF-built material, their size is significantly smaller than that of cast materials and raw material powder, reflecting the high cooling rate of L-PBF. Almost no concentration segregation occurs, proving that ultra-quenching peculiar to L-PBF is an extremely effective means of suppressing elemental segregation, followed by the phase separation of BioHEAs.[38]

Figure 7 shows the crystallographic texture formed using the L-PBF method. The inverse pole figure (IPF) maps in Fig. 7, which were obtained by observing the YZ cross-section of the sample, shows the crystal orientation in the building direction (BD). The cast material comprises coarse grains with random orientation. The L-PBF-built material shows a bimodal structure consisting of fine equiaxed grains with an average of approximately 250 nm near the outer edge of the molten pool and columnar crystal structure (width: 2.5 µm, length: 31 µm) in the central part of the molten pool, where ⟨001⟩ is oriented parallel to the BD without preferential orientation toward the other directions.

L-PBF can produce complex shapes as generally known. It has recently been shown that the crystallographic texture (including polycrystal to single crystal formation) and crystal orientation can be artificially controlled based on the scanning strategy of the laser[39–42] (Fig. 8). Particularly, by applying the XY scan strategy, which is the alternately repeated laser scan along the X- and Y-axes for each layer, most cubic metals have a single crystal-like structure in which {001} is preferentially oriented for any of the X-, Y-, and Z-axes (Fig. 8(b)). To form this single crystal-like structure, it is indispensable to take over the crystallographic texture along the BD from the lower to the upper layer by epitaxial growth driven by a decrease in the interfacial energy in the entire system. However, in the case of the
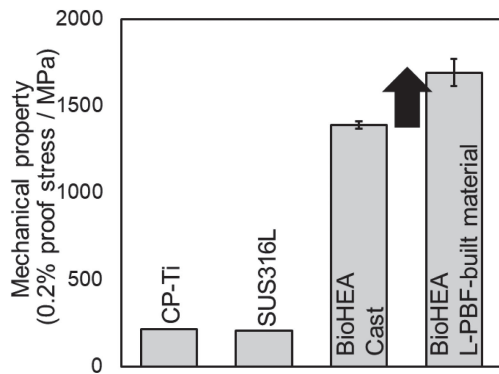
Fig. 9 Improvement of mechanical properties in $(TiZr)_{1.4}(NbTaMo)_{0.6}$ alloy (BioHEA) fabricated using the L-PBF method. $*$: $P < 0.05$. This figure cites Ref. 38) with a minor modification.

$(TiZr)_{1.4}(NbTaMo)_{0.6}$ alloy, when the solidified layer is remelted through laser irradiation, the dendrite structure is mainly composed of high melting points of Nb, Mo, and Ta that do not melt. Alternatively, the high melting point phase that precipitates and becomes a nucleation site in the molten pool so that the crystal grains become finer at the bottom of the molten pool.[43] Consequently, the transfer of the crystal orientation from the lower layer is hindered, and a single crystal-like structure is not formed. This can be understood from the fact that the length of the columnar crystals in the BD ($31\,\mu m$) is smaller than the powder bed stacking thickness in each layer ($60\,\mu m$).

The obtained L-PBF-built material shows a higher 0.2% proof stress than existing metal biomaterials, such as pure Ti and SUS316L, as well as the cast of $(TiZr)_{1.4}(NbTaMo)_{0.6}$ alloy (Fig. 9).[38] The possible factors for this include grain refinement strengthening, solid-solution hardening derived from the forced solid solution, and cellular structure strengthening. Figure 10 shows the results of cell proliferation tests using primary osteoblasts. Clearly, Giemsa stain images (Fig. 10(a)) and the quantitative analysis result of the adhesion cell density (Fig. 10(b)) that the biocompatibility of the $(TiZr)_{1.4}(NbTaMo)_{0.6}$ alloy does not depend on the alloy manufacturing method; it is approximately the same as that of pure Ti and is higher than that of SUS316L.[38] Here, the area of adherent cells in the L-PBF-built material is significantly higher than that of the cast material (Fig. 10(c)). In the cast $(TiZr)_{1.4}(NbTaMo)_{0.6}$ alloy with significant elemental segregation, osteoblast adhesion is limited to the Ti-enriched inter-dendrite region. However, in the L-PBF-built material, elemental segregation of Ti hardly occurs; thus, the adhesive region is not limited. Consequently, osteoblasts are considered to improve the cell adhesion area of the L-PBF-built material compared to that of the cast material. These results indicate that the creation of a single-phase solid solution is important for the functional expression of the $(TiZr)_{1.4}(NbTaMo)_{0.6}$ alloy. Further, ultra-rapid solidification in the L-PBF method is an extremely effective means of forming BioHEAs with original functionality.

5. Conclusion

Although recently developed BioHEAs are excellent biomaterials that exhibit high biocompatibility and mechanical properties, the original potential of alloys produced using conventional casting methods cannot be fully exhibited because of elemental segregation and phase separation. In this review, we introduced BioHEAs that suppress elemental segregation by utilizing ultra-rapid solidification via the L-PBF method. From the viewpoint of alloy design, attempts have been made to introduce the d-electron alloy design theory cultivated in the research of Ti alloys and the Mo equivalent into the composition design of BioHEAs, tending to suppress segregation even in cast materials. In the future, BioHEAs that have an ideal uniform solid solution state can be developed by combining ultra-rapid cooling using the L-PBF method and a new alloy design method.
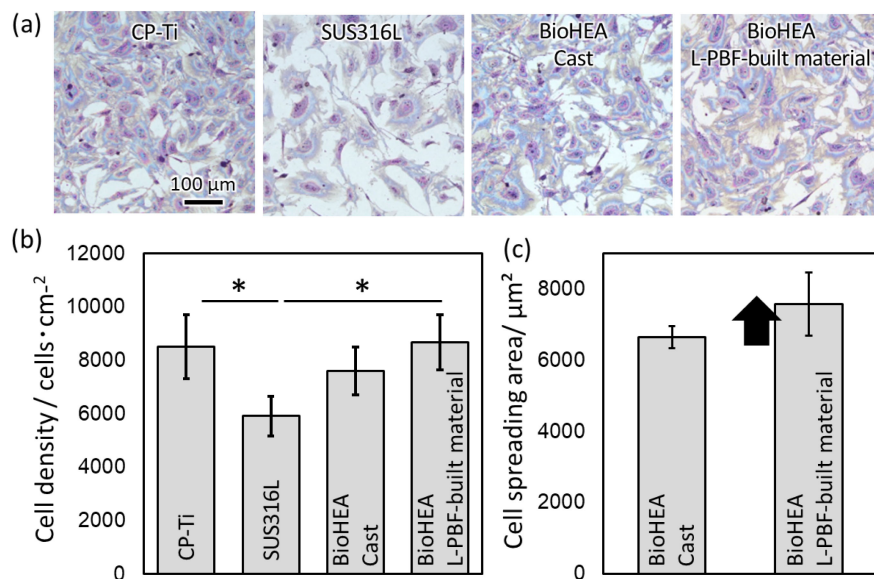

Fig. 10 Improved biocompatibility in $(TiZr)_{1.4}(NbTaMo)_{0.6}$ alloy (BioHEA) fabricated using the L-PBF method. (a) Giemsa-stained images of osteoblasts on a metal substrate. Quantitative results of (b) cell density and (c) cell spreading area. $*$: $P < 0.05$. This figure cites Ref. 38) with a minor modification.

Acknowledgments

REFERENCES

1) B. Cantor, I.T.H. Chang, P. Knight and A.J.B. Vincent: Mater. Sci. Eng. A **375–377** (2004) 213–218.
2) J.-W. Yeh and S.-Y. Chang: Adv. Eng. Mater. **6** (2004) 299–303.
3) M. Todai, T. Nagase, T. Hori, A. Matsugaki, A. Sekita and T. Nakano: Scr. Mater. **129** (2017) 65–68.
4) T. Nagase, M. Todai, T. Hori and T. Nakano: J. Alloy. Compd. **753** (2018) 412–421.
5) T. Nagase, K. Mizuuchi and T. Nakano: Entropy **21** (2019) 483.
6) T. Hori, T. Nagase, M. Todai, A. Matsugaki and T. Nakano: Scr. Mater. **172** (2019) 83–87.
7) T. Nagase, M. Todai and T. Nakano: Scr. Mater. **186** (2020) 242–246.
8) T. Nagase, Y. Iijima, A. Matsugaki, K. Ameyama and T. Nakano: Mater. Sci. Eng. C **107** (2020) 110322.
9) Y. Iijima, T. Nagase, A. Matsugaki, P. Wang, K. Ameyama and T. Nakano: Mater. Des. **202** (2021) 109548.
10) G. Popescu, B. Ghiban, C.A. Popescu, L. Rosu, R. Truscă, I. Carcea, V. Soare, D. Dumitrescu, I. Constantin, M.T. Olaru and B.A. Carlan: IOP Conf. Series **400** (2018) 022049.
11) Y. Yuan, Y. Wu, Z. Yang, X. Liang, Z. Lei, H. Huang, H. Wang, X. Liu, K. An, W. Wu and Z. Lu: Mater. Res. Lett. **7** (2019) 225–231.
12) A. Motallebzadeh, N.S. Peighambardoust, S. Sheikh, H. Murakami, S. Guo and D. Canadinc: Intermetallics **113** (2019) 106572.
13) H. Song, S. Lee and K. Lee: Int. J. Refract. Met. Hard Mater. **99** (2021) 105595.
14) M. Calin, J. Vishnu, P. Thirathipviwat, M.-M. Popa, M. Krautz, G. Manivasagam and A. Geberta: Mater. Sci. Eng. C **121** (2021) 111733.
15) Y.J. Hsu, W.C. Chiang and J.K. Wu: Mater. Chem. Phys. **92** (2005) 112–117.
16) B. Ren, Z.X. Liu, D.M. Li, L.Q. Shi, B. Cai and M.X. Wang: Mater. Corros. **63** (2012) 828–834.
17) Y. Qiu, S. Thomas, M.A. Gibson, H.L. Fraser and N. Birbilis: npj Mater. Degrad. **1** (2017) 15.
18) B.S. Murty, J.-W. Yeh and S. Ranganathan: *High-Entropy Alloys*, 1st ed., (Elsevier, Amsterdam, 2014).
19) M.C. Gao, J.-W. Yeh, P.K. Liaw and Y. Zhang: *High-Entropy Alloys, Fundamentals and Applications*, 1st ed., (Springer, Berlin, 2016).
20) S. Guo, C. Ng, J. Lu and C.T. Liu: J. Appl. Phys. **109** (2011) 103505.
21) A. Takeuchi and A. Inoue: Mater. Trans. **46** (2005) 2817–2829.
22) Q. Jia, P. Rometsch, P. Kürnsteiner, Q. Chao, A. Huang, M. Weyland, L. Bourgeois and X. Wu: Acta Mater. **171** (2019) 108–118.
23) D. Gu, Q. Shi, K. Lin and L. Xi: Addit. Manuf. **22** (2018) 265–278.
24) E. Lee and B. Mishra: Mater. Trans. **58** (2017) 1624–1627.
25) T. Nagase, M. Takemura, M. Matsumuro and T. Maruyama: Mater. Trans. **59** (2018) 255–264.
26) R.W. Cahn: *Physical Metallurgy*, third ed., (Elsevier Science Publishers, North-Holland, 1996).
27) S.-H. Sun, T. Ishimoto, K. Hagihara, Y. Tsutsumi, T. Hanawa and T. Nakano: Scr. Mater. **159** (2019) 89–93.
28) N. Ikeo, H. Fukuda, A. Matsugaki, T. Inoue, A. Serizawa, T. Matsuzaka, T. Ishimoto, R. Ozasa, O. Gokcekaya and T. Nakano: Crystals **11** (2021) 959.
29) N. Ikeo, T. Matsumi, T. Ishimoto, R. Ozasa, A. Matsugaki, T. Matsuzaka, O. Gokcekaya, Y. Takigawa and T. Nakano: Crystals **11** (2021) 1074.
30) R. Ozasa, T. Ishimoto, S. Miyabe, J. Hashimoto, M. Hirao, H. Yoshikawa and T. Nakano: Calcif. Tissue Int. **104** (2019) 449–460.
31) R. Ozasa, A. Matsugaki, T. Ishimoto, S. Kamura, H. Yoshida, M. Magi, Y. Matsumoto, K. Sakuraba, K. Fujimura, H. Miyahara and T. Nakano: Bone **155** (2022) 116261.
32) T. Moriishi, R. Ozasa, T. Ishimoto, T. Nakano, T. Hasegawa, T. Miyazaki, W. Liu, R. Fukuyama, Y. Wang, H. Komori, X. Qin, N. Amizuka and T. Komori: PLoS Genet. **16** (2020) e1008586.
33) T. Nakano, K. Kaibara, Y. Tabata, N. Nagata, S. Enomoto, E. Marukawa and Y. Umakoshi: Bone **31** (2002) 479–487.
34) W.J. Sames, F.A. List, S. Pannala, R.R. Dehoff and S.S. Babu: Int. Mater. Rev. **61** (2016) 315–360.
35) H. Amano, T. Ishimoto, R. Suganuma, K. Aiba, S.-H. Sun, R. Ozasa and T. Nakano: Addit. Manuf. **48** (2021) 102444.
36) T. Ishimoto, S. Wu, Y. Ito, S.-H. Sun, H. Amano and T. Nakano: ISIJ Int. **60** (2020) 1758–1764.
37) O. Gokcekaya, T. Ishimoto, S. Hibino, J. Yasutomi, T. Narushima and T. Nakano: Acta Mater. **212** (2021) 116876.
38) T. Ishimoto, R. Ozasa, K. Nakano, M. Weinmann, C. Schnitter, M. Stenzel, A. Matsugaki, T. Nagase, T. Matsuzaka, M. Todai, H.S. Kim and T. Nakano: Scr. Mater. **194** (2021) 113658.
39) T. Ishimoto, K. Hagihara, K. Hisamoto, S.-H. Sun and T. Nakano: Scr. Mater. **132** (2017) 34–38.
40) S.-H. Sun, K. Hagihara and T. Nakano: Mater. Des. **140** (2018) 307–316.
41) T. Ishimoto, K. Hagihara, K. Hisamoto and T. Nakano: Addit. Manuf. **43** (2021) 102004.
42) K. Hagihara, T. Ishimoto, M. Suzuki, R. Ozasa, A. Matsugaki, P. Wang and T. Nakano: Scr. Mater. **203** (2021) 114111.
43) H. Zhang, D. Gu, J. Yang, D. Dai, T. Zhao, C. Hong, A. Gasser and R. Poprawe: Addit. Manuf. **23** (2018) 1–12.